

# Synthesis of Ordered Mixed Titania and Silica Mesostructured Monoliths for Gold Catalysts

Haoguo Zhu, Zhengwei Pan, Bei Chen, Byunghwan Lee, Shannon M. Mahurin, Steven H. Overbury, and Sheng Dai\*

Chemical Sciences Division, Oak Ridge National Laboratory, Oak Ridge, Tennessee 37831-6201

Received: June 8, 2004; In Final Form: October 13, 2004

Mesostructured silica–titania mixed oxide monoliths, in which the nanocrystalline titania is well dispersed inside the silicate framework, have been synthesized by a liquid crystalline templating approach in combination with sol–gel processing. Control over the different hydrolysis and condensation rates of silicon and titanium alkoxides was achieved by complexation of the titanium species to the poly(ethylene oxide) (PEO) part of a block copolymer, such as Pluronic F108. The block copolymer serves two distinct functions: (a) as a structure-directing agent and (b) as a moderator of the hydrolysis rate of titanium alkoxide. The amorphous titania inside the silica framework is converted by calcination treatment into anatase phase  $\text{TiO}_2$  incorporated on the silica. The structure and composition of the resulting material was characterized by X-ray diffraction, UV–visible absorption spectroscopy, Raman spectroscopy, and transmission electron microscopy. The monoliths have an ordered mesostructure with very small crystallites of anatase  $\text{TiO}_2$  located within the mesopores. We show that the mixed oxide monoliths are excellent support materials for gold catalysts.

## Introduction

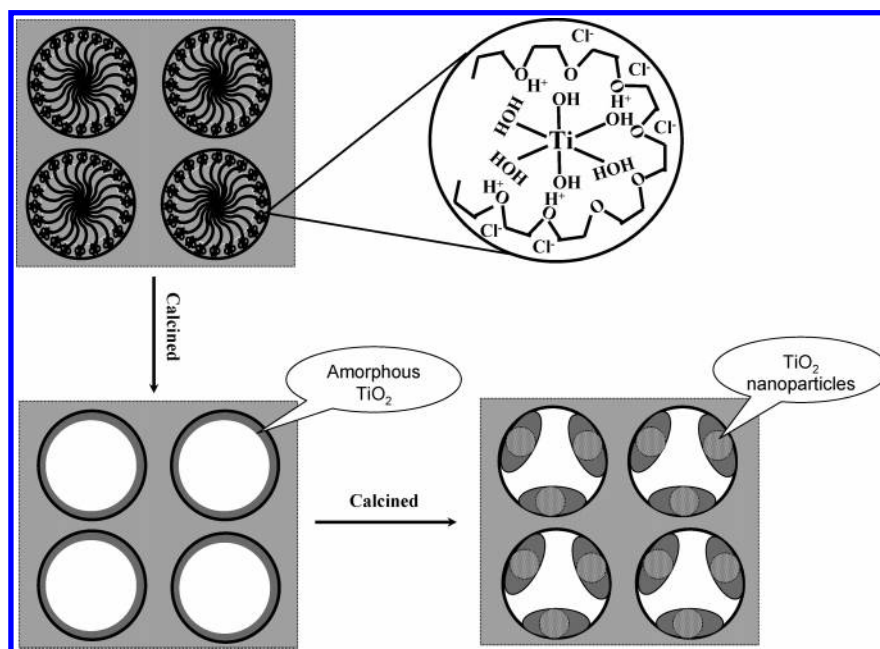
Titanium dioxide,  $\text{TiO}_2$ , which is one of the most widely studied metal oxides, attracted significant attention as early as 1972 when Fujishima and Honda discovered that  $\text{TiO}_2$  can catalyze the photochemical splitting of water.<sup>1</sup> Following the discovery of Fujishima and Honda, extensive research efforts have been focused on understanding the photocatalytic behavior of  $\text{TiO}_2$  and other semiconducting oxides.<sup>2</sup> Among semiconducting oxides, the nanostructured materials based on  $\text{TiO}_2$  are still the most effective in a wide range of applications including solar energy conversion,<sup>3,4</sup> improved catalysts,<sup>5</sup> and environmental pollution remediation.<sup>6</sup> Notably, Haruta and co-workers have recently found that powdered  $\text{TiO}_2$  nanoparticles are very effective in supporting gold catalysts, which are active for the catalytic oxidation of carbon monoxide at subambient conditions.<sup>7</sup> The key drawbacks associated with powdered  $\text{TiO}_2$  in a number of the above applications are (1) limited light transmission due to scattering, (2) limited surface areas, and (3) susceptibility to sintering. These deficiencies have prompted us to search for alternative  $\text{TiO}_2$  systems that can overcome the above limitations.

Recent breakthroughs in the synthesis of mesoporous materials have led to a new class of the mesoporous materials with ordered mesopores and extremely high surface areas.<sup>8–13</sup> The essence of this methodology involves the use of molecular assemblies of surfactants or related substances as structure directors during formation of oxides. Mesoporous  $\text{TiO}_2$  with high surface areas has been prepared via such a self-assembly method.<sup>9,13</sup> The ordered mesostructures formed in the case of metal oxides other than silica are more susceptible to the collapse of pore structures with high-temperature treatments. This destruction of the ordered mesoscopic structures has been ascribed to the crystallization of the amorphous metal oxide phase, frequently leading to solids with no ordered mesophases. Although a majority of the metal oxides can be prepared in

high-surface area mesoporous forms with the above methodologies, very few robust, *ordered* mesoporous materials with crystalline wall structures have been obtained to date.<sup>14</sup> An alternative is to incorporate metal oxides (e.g., titania) into more mechanically and thermally stable ordered amorphous silica frameworks. To date, most reported results for titanium-substituted mesoporous silica materials are for selective oxidations of organic compounds in the presence of hydrogen peroxide, where amorphous titanium species are dispersed in silica matrixes.<sup>15–18</sup> Our objective is to produce ordered mixed silica–titania mesostructured monoliths by a sol–gel process and subsequent calcination to induce controlled nucleation and growth of *stable*  $\text{TiO}_2$  nanocrystals from the corresponding amorphous silica matrixes.

Herein, we report the synthesis of binary mesoporous oxide monoliths and further preparation of mesostructured materials containing high-temperature stable  $\text{TiO}_2$  nanocrystals via a co-assembly approach. The co-assembly approach used in our synthesis is based on an  $\text{I}^+ \text{X}^- \text{S}^+$  scheme using a block copolymer as a structure-directing agent for the synthesis of mesoporous supports in an acid medium.<sup>19</sup> The positively charged surfactant molecules ( $\text{S}^+$ ), such as protonated block copolymers, interact with positively charged siliceous species ( $\text{I}^+$ ) through a negatively charged mediator  $\text{X}^-$ . Accordingly, the positively charged molecules ( $\text{S}^+$ ) in this case can be both protonated block copolymers and cationic metal complexes. The multivalent metal species ( $\text{M}^+$ ) can associate preferentially with the hydrophilic poly(ethylene oxide) (PEO) mediated by HCl. The alkylene oxide segments can form crown-ether-type complexes with inorganic ions through weak coordination bonds and hydrogen bonds.<sup>9,20</sup> Their preferential location in the hydrophilic phase of surfactants may prevent excessive disruption of the silica wall during the formation of the mesostructure. The overall reaction is shown in Scheme 1. In this paper, synthetic procedures were extended to achieve an ordered large area silica–titania mixed metal oxide monolith with a large pore

SCHEME 1



diameter using a block copolymer as the structure-directing agent. The temperature and calcination time should determine the characteristics of  $\text{TiO}_2$  nanocrystals, which can provide new supports for gold catalysts.<sup>21–24</sup> Such mixed oxide materials would take advantage of the high thermal stability and excellent mechanical strength of  $\text{SiO}_2$  and the active support properties of  $\text{TiO}_2$ . In addition, this approach provides significantly more flexibility in processing and makes possible the preparation of mesostructured binary monoliths,<sup>25–28</sup> thin films,<sup>29</sup> and fibers<sup>30</sup> in addition to powders.

## Experimental Section

**Synthesis.** Mixed mesoporous metal oxide monoliths were synthesized as follows: 2 mL of titanium(IV) tetraethoxide (for Si/Ti=5.5) was dissolved in 5.4 g of F108 ( $\text{EO}_{130}\text{PO}_{60}\text{EO}_{130}$ ) and 42 mL of ethanol in the presence of 1.6 mL of concentrated hydrochloric acid at room temperature under vigorous stirring. After 10–15 min, this solution was mixed with a solution of 10.0 g of tetraethyl orthosilicate (TEOS) hydrolyzed in 6.4 g of 0.1 M HCl. After further stirring for several hours, the solution was transferred to Petri dishes and left to dry under ambient conditions (generally, several hours). After gelation for several days, the transparent and continuous monolith was calcined in air to remove the surfactant molecules. Each sample was ramped to 350 °C (at 1 °C/min) and held for 3 h before ramping to the final calcination temperature and holding for another 5 h.

**Gold Deposition–Precipitation.** The introduction of the gold precursor was achieved by a deposition–precipitation (DP) process.<sup>7</sup> Briefly, a 50 mL aqueous solution containing 0.148 g of  $\text{HAuCl}_4 \cdot 3\text{H}_2\text{O}$  was mixed under vigorous stirring with 0.7 g of the calcined mesoporous titania–silica material. The pH value of the resulting mixture solution was adjusted to a pH of 7 using a 5.0 wt % KOH solution at 60 °C. After the DP process for 2 h, the sample was centrifuged and washed. Finally, the powder was dried at 40 °C for 12 h.

**Catalytic Activity Measurements.** Steady-state activity measurements for the oxidation of CO were carried out in a 0.35 mL a fixed bed silica tube microreactor at ambient pressure. Typically, 50 mg of catalyst material was packed in the middle

of the reactor and supported by quartz wool. A gas stream of 1% CO balanced with dry air (<4 ppm water) flowed through the catalyst at 37  $\text{cm}^3/\text{min}$  (i.e., GHSV = 40 000  $\text{h}^{-1}$ ). The gas samples were analyzed periodically by gas chromatography, with the CO conversion defined as the ratio of the moles of CO consumed to the initial moles of CO.

**Characterization Techniques.** The prepared samples were characterized using a nitrogen adsorption–desorption measurement (Autosorb-1, Quantachrome) to examine surface area and pore structure. The imaging studies were performed using a HD-2000 scanning transmission electron microscope operating at 200 kV. The powder X-ray diffraction patterns of the samples were recorded using a SIEMENS D5005 X-ray diffractometer, where a Cu target  $\text{K}\alpha$  ray ( $\lambda = 0.154$  nm and operating at 40 kV and 40 mA) was used as the X-ray source. UV–vis spectroscopic measurements were carried out on a UV–visible spectrophotometer (Cary 4E, Varian). The collected relative reflection intensity ( $R_\infty = R_{\text{sample}}/R_{\text{reference}}$ ) was transformed into  $F(R_\infty)$  by using the Kubelka–Munk function  $F(R_\infty) = (1 - R_\infty)/2(1 + R_\infty)$ ,<sup>31</sup> all spectra were plotted in terms of  $F(R_\infty)$  versus wavelength. Raman spectra were recorded with a Renishaw system 1000 Raman spectrometer equipped with an integral microscope (Leica DMLMS/N). Radiation of 632.8 nm from a 25 mW air-cooled He–Ne laser (Renishaw) was used as the excitation source. Raman scattering was collected with a  $50 \times 0.75$  NA dry objective in 180° configuration and focused into a Peltier-cooled CCD camera ( $400 \times 600$  pixels). With a holographic grating ( $1800$  grooves  $\cdot \text{cm}^{-1}$ ) and a 50  $\mu\text{m}$  slit, a spectral resolution of 1  $\text{cm}^{-1}$  can be obtained. A silicon wafer with a Raman band at 520  $\text{cm}^{-1}$  was used to calibrate the spectrometer.

## Result and Discussion

Nanosized oxide particles are generally introduced onto presynthesized mesoporous materials using chemical vapor deposition<sup>32,33</sup> or covalent grafting of ligands including metal complexes<sup>34</sup> and organometallic compounds.<sup>35</sup> An alternative technique (a potentially easier approach) is a coassembly methodology.<sup>36–40</sup> One problem associated with this approach, however, is the unequal hydrolysis rates of the metal alkoxide

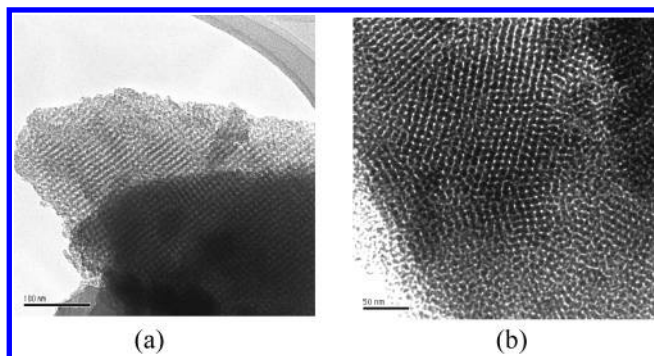


**Figure 1.** TEM image of the calcined sample of Si/Ti = 5.5 (a) and Si/Ti = 3.7 (b) (molar ratio).

precursors. Titanium ethoxide  $[\text{Ti}(\text{OEt})_4]$  is well-known to hydrolyze faster than silicon alkoxides.<sup>41</sup> Consequently, the addition of titanium alkoxide to a sol, which is designed for the formation of well-structured silica, typically results in an instantaneous precipitation of titanium oxide.

One solution to this problem is the coordination of the reactive titanium precursor to the surfactant hydrophilic headgroup, which slows the hydrolysis rate of titanium alkoxide.<sup>42</sup> Thus, the mobility and reactivity of titanium precursors is strongly hindered, which reduces the aggregation of hydrolyzed titanium oxide particles. Recently, Dag et al. reported a new hexagonal and/or cubic lyotropic liquid crystalline phase prepared using nonionic oligo(ethylene oxide) surfactants and metal salts.<sup>43</sup> The interaction between metal ions and alkylene oxide segments ensures the dispersion of metal atoms throughout the nascent mesophase. It is possible to prepare complex mesoporous oxide materials using this kind of lyotropic liquid crystalline phase as a template. Husing et al. has reported the preparation of mesostructured silica–titania mixed metal oxide films,<sup>42</sup> and Wiesner et al. synthesized a mesoporous mixed oxide containing  $\gamma\text{-Fe}_2\text{O}_3$  nanoparticles with this method.<sup>36</sup>

We report the synthesis of ordered mesoporous mixed oxide monoliths using poly(ethylene oxides)-*b*-poly(propylene oxides)-*b*-poly(ethylene oxides) (PEO–PPO–PEO) EO<sub>130</sub>PO<sub>60</sub>EO<sub>130</sub> (F108) as the structure-directing agent in acidic conditions with titanium ethoxide and tetraethyl orthosilicate (TEOS) as the inorganic species precursors. As for the siliceous monolith, silica–titania mesostructured materials can be obtained as an optically transparent monolith with large area. The dried monolith is flexible and can be cut into any desired shape. The optical transparency of such monoliths was retained even after calcination. The representative TEM images of Si/Ti = 5.5 and 3.7 shown in Figure 1 reveal that these mesoporous mixed metal oxides have well-defined cubic mesostructure.<sup>44,45</sup> Long-range structural ordering is maintained via direct mixed-gel synthesis for relatively high titanium loading.

To elucidate the location of the titanium species in the mixed oxide mesostructure, XRD experiments were performed on two samples synthesized as follows: (a) condensation from the inorganic precursors with the block copolymer and (b) a simple mechanical mixture of mesophase titania and mesophase silica with the block copolymer. Both samples were heated to 700 °C in air, and in each case the molar ratio was Si/Ti = 5.5. The wide angle XRD patterns of the calcined samples are compared in Figure 2. The first sample exhibits a broad scattering peak of amorphous silica at  $2\theta \sim 22^\circ$  with a poorly crystalline anatase titania phase (Figure 2a). It should be noted that the formation of the anatase phase titania in mesoporous  $\text{SiO}_2\text{--TiO}_2$  is similar to that in titania-modified mesoporous materials by solution-phase grafting.<sup>34,46,47</sup> A simple mixture of mesoporous silica

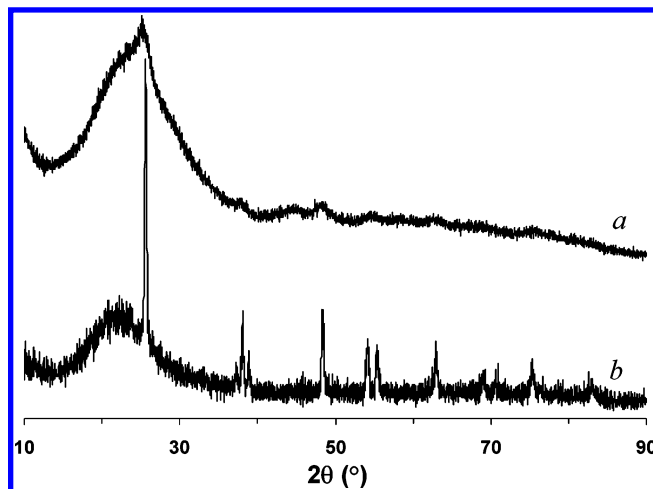


**Figure 2.** XRD patterns of the sample of mesoporous mixed titania–silica (a) and mechanically mixed mesoporous titania and silica (b) calcined at 700 °C (Si/Ti = 5.5).

and titania (anatase) show intense peaks due to the well-developed crystals of anatase titania phase (Figure 2b) superimposed upon the amorphous silica. The block copolymer induces the  $\text{SiO}_2\text{--TiO}_2$  heterostructure to produce phase separation on a nanoscale, but elemental mapping by EDAX demonstrates a homogeneous dispersion of titanium throughout the silica matrix because of the limited resolution of TEM.

With an increase in the titanium content, the amount of  $\text{Ti}^{4+}$  cations in the silica matrix increases. As a result of calcination, amorphous titania begins to crystallize, nucleating the crystalline  $\text{TiO}_2$  phase within the silica, in the pores or on the silica surface. The XRD patterns of the mixed silica–titania materials following calcination at 600 °C are shown in Figure 3a. An XRD spectrum from mesoporous silica is shown for comparison with the positions of crystalline  $\text{TiO}_2$  (anatase) indicated by dashed lines. The formation of *only* anatase phase  $\text{TiO}_2$  is consistent with the stability data concerning the nanoparticles of  $\text{TiO}_2$ . Among three  $\text{TiO}_2$  allotrope phases, anatase is the most stable phase for nanocrystalline  $\text{TiO}_2$  based on the work by Navrotsky and co-workers.<sup>48</sup> Contrarily, rutile is the most stable phase for bulk  $\text{TiO}_2$ . The anatase phase can be readily converted to the rutile phase through calcination of bulk anatase or pure anatase nanoparticles. In our binary oxide case, the anatase nanocrystals are entrapped and isolated inside the silica networks so that the aggregation of the nanoparticles is considerably hindered, leading to an extremely stable anatase  $\text{TiO}_2$ .

At low Ti concentration, only the broad peak due to the amorphous matrix is observable. With increasing Ti loading, the anatase reflections at  $2\theta = 37.8, 53.9, 62.7,$  and  $75.0^\circ$  become more visible in the pattern, indicating the development of crystallinity and an increase in anatase  $\text{TiO}_2$  particle size. By using the Scherrer diffraction formula ( $d = \kappa\lambda/\beta \cos \theta$ ),<sup>49</sup> the crystallite sizes are calculated to be about 1.8, 6.0, and 6.4 nm for Si/Ti molar ratios of 6.0, 3.7, and 2.7, respectively. No crystalline features could be detected by XRD in the samples of Si/Ti = 10, thus indicating mixing of amorphous Ti and Si components in this material. The formation of smaller nanoparticles at low Ti concentration in the monolith also contributes to the homogeneous dispersion of the Ti throughout the monolith structure.

As expected, the extent of crystallization increases with calcination temperature, as demonstrated by the XRD patterns in Figure 4a for the sample with a Si/Ti ratio of 5.5. No anatase features are visible after calcination at 500 °C, but small weak



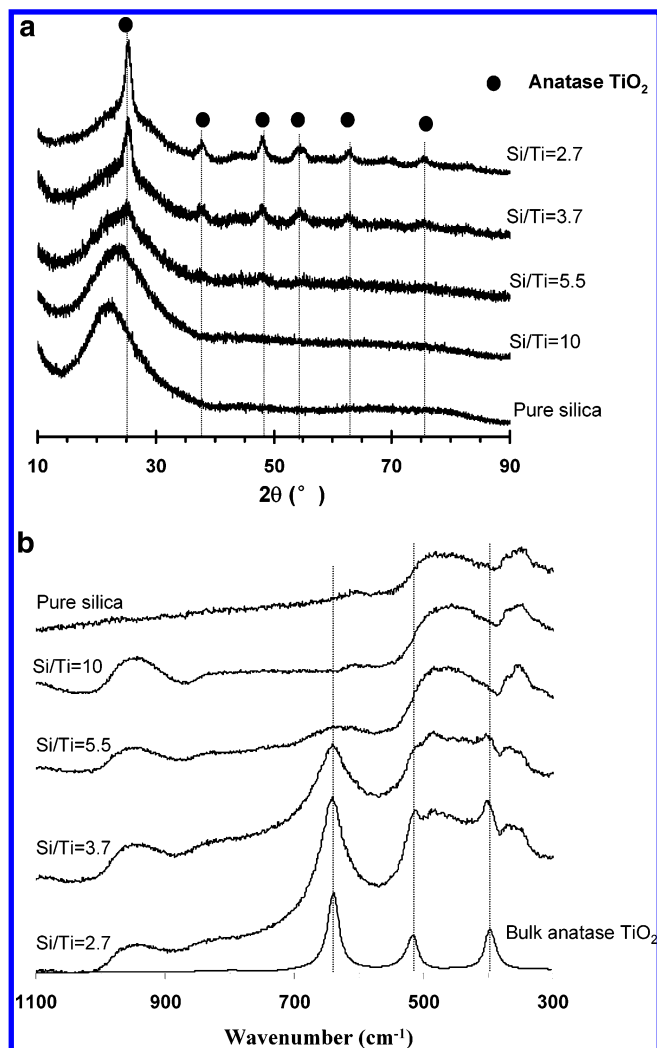


**Figure 3.** (a) XRD patterns of different samples calcined at 600 °C with different content of titania. (b) Raman spectra of the sample calcined at 600 °C with different content of titania.

reflections at  $2\theta = 25.2$  and  $48.1^\circ$  appear in the pattern after calcination at 700 °C. The lack of features at the lower temperature further indicates a homogeneous distribution of the titanium species in an amorphous phase. Calcination at 700 °C promotes growth of the TiO<sub>2</sub> crystallites causing a sharpening of the anatase features, which makes them more prominent in the XRD.

Raman spectroscopy is much more sensitive to the crystalline TiO<sub>2</sub> (anatase) phase than to the amorphous phase in SiO<sub>2</sub>-TiO<sub>2</sub> because of its strong scattering properties associated with ordered lattice structures. Figure 3b shows the Raman spectra of the mixed titania-silica mesoporous materials with varying titanium content, all calcined to 600 °C. A broad band at 430 cm<sup>-1</sup> observed for pure silica may be assigned to a combination of Si-O-Si and O-Si-O bond bending vibrations.<sup>50</sup> As the Ti loading increases, significant changes in the spectrum occur. At all Ti concentrations a broad band at 950 cm<sup>-1</sup> is present. It is assigned to an asymmetric stretch of the Si-O-Ti bond sequence, involving tetrahedrally coordinated Ti<sup>4+</sup> ions.<sup>50</sup> Raman bands at 397, 515, and 639 cm<sup>-1</sup> characteristic of anatase TiO<sub>2</sub> were detected for samples with high Ti loading. The growth of these features indicates an increase in anatase concentration with increasing TiO<sub>2</sub> content, in agreement with the XRD results. The Raman spectra suggest that tetrahedral Ti<sup>4+</sup> is present at all concentrations but that there is a limit to the amount that

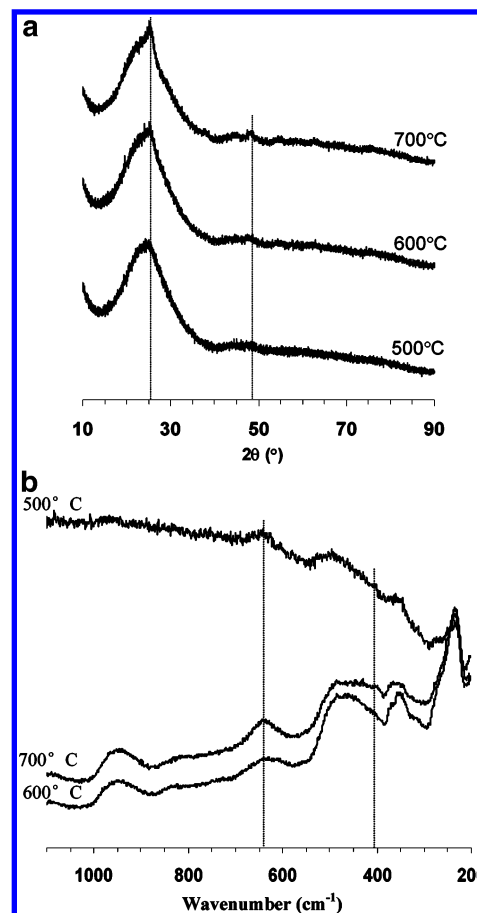


**Figure 4.** (a) XRD patterns of the sample with Si/Ti = 5.5 calcined at different temperature. (b) Raman spectra of the sample with Si/Ti = 5.5 calcined at different temperature.

may be incorporated into the tetrahedral network. When this limit is exceeded, amorphous TiO<sub>2</sub>-rich regions are formed that are more susceptible to crystallization during calcination treatment. The effect of calcination at increasing temperatures is shown in Figure 4b for the molar ratio of Si/Ti = 5.5. After calcination at 500 °C, a strong background is observed due to fluorescence from residual surfactants; however, the peak at 397 cm<sup>-1</sup> due to anatase remains visible. The peaks at 397 and 639 cm<sup>-1</sup> assigned to anatase gradually become stronger as the calcination temperature increases, consistent with an increase in the amount of crystalline anatase. The observed Raman spectrum resembles that previously reported for fumed silica coated with titanium dioxide.<sup>51</sup>

The UV absorption threshold or optical band gap of titania is known to be a strong function of particle size for diameters less than 10 nm, an effect that can be attributed to the well-known quantum size effect.<sup>52,53</sup> Figure 5 shows the diffuse reflectance UV-visible spectra of samples with different Ti content calcined at 600 °C. The spectra are referenced to a pure mesoporous silica. As the Ti content increases, the UV absorption edge shifts to longer wavelength. The sample with Si/Ti = 10 shows an absorption band centered at 220 nm and a shoulder at 270 nm. The absorption band at 220 nm is attributed to four-coordinate Ti,<sup>54,55</sup> whereas the band at 270 nm has been attributed to five- and six-coordinate Ti.<sup>56</sup> In the spectra of the samples with Si/Ti = 5.5, 3.7, and 2.7, the broad absorption band shifts to higher wavelength and becomes more similar to the anatase spectrum. This shift indicates that the Ti atoms are not completely isolated in the silica framework but exist as Ti-O-Ti linkages in Ti-rich microdomains that grow

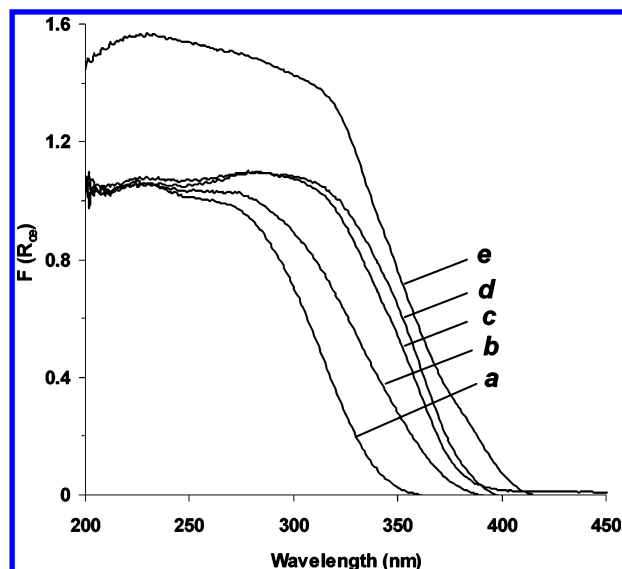


**Figure 5.** Diffuse reflectance UV-vis spectra of the samples calcined at 600 °C with different content of titania (molar ratio) (a) Si/Ti = 10, (b) Si/Ti = 5.5, (c) Si/Ti = 3.7, (d) Si/Ti = 2.7, and (e) bulk anatase  $\text{TiO}_2$ .

progressively larger with increasing Ti content. These shifts might indicate the existence of a small amount of the anatase phase in the silica matrix, in agreement with the XRD and Raman results.

A band edge of 339–383 nm, obtained by extrapolating the steep slope of the absorption curves to zero intensity, is observed for the Si/Ti mixed oxide compared to a band edge of 386 nm (3.25 eV) for bulk anatase. The blue shift of the silica–titania band edge compared to pure anatase is caused by quantum size effects that are observed in semiconductors as the particle size decreases. In titania, a large-band gap semiconductor, particle sizes below 10 nm in diameter are sufficient to induce the optical confinement effects that generate the increased band gap energy. Therefore, in these mixed oxides, the titania must be present as crystallized domains less than 10 nm. The blue shift diminishes with increased titania loading, implying an increase in the crystallized titania domains. In the samples of Si/Ti = 10 exhibiting a band edge of 339 nm, no trace of anatase titania was observed in the powder XRD patterns and Raman spectra. With increasing titania loading, the characteristic anatase XRD reflections become more prominent (Figure 3a), and the band edge gradually approaches the semiconductor band gap energy of crystalline bulk anatase.

Nitrogen adsorption/desorption isotherms of the silica–titania monolith calcined to 600 °C are shown in Figure 6a. The isotherms all show type IV curves with a typical H2 hysteresis loop, which implies that the samples have large mesopores with windows or necks.<sup>57</sup> The Brunauer–Emmett–Teller (BET) surface area and volume of pores significantly decreased with increasing titanium content. Table 1 lists the changes in volume of absorbed saturation, surface area, and pore volume for several representative samples.

The sharpness and height of the capillary condensation (pore filling) step in the isotherms is a measure of the pore-size uniformity.<sup>57</sup> Departures from a sharp and clearly defined pore filling step are usually an indication of greater pore-size heterogeneity (i.e., broadening of pore size distribution). Both the pure silica and Ti-containing samples exhibit isotherms with a well-developed step in the relative pressure ( $P/P_0$ ) range 0.4–0.7, characteristic of capillary condensation into uniform mesopores. However, the capillary condensation step is much

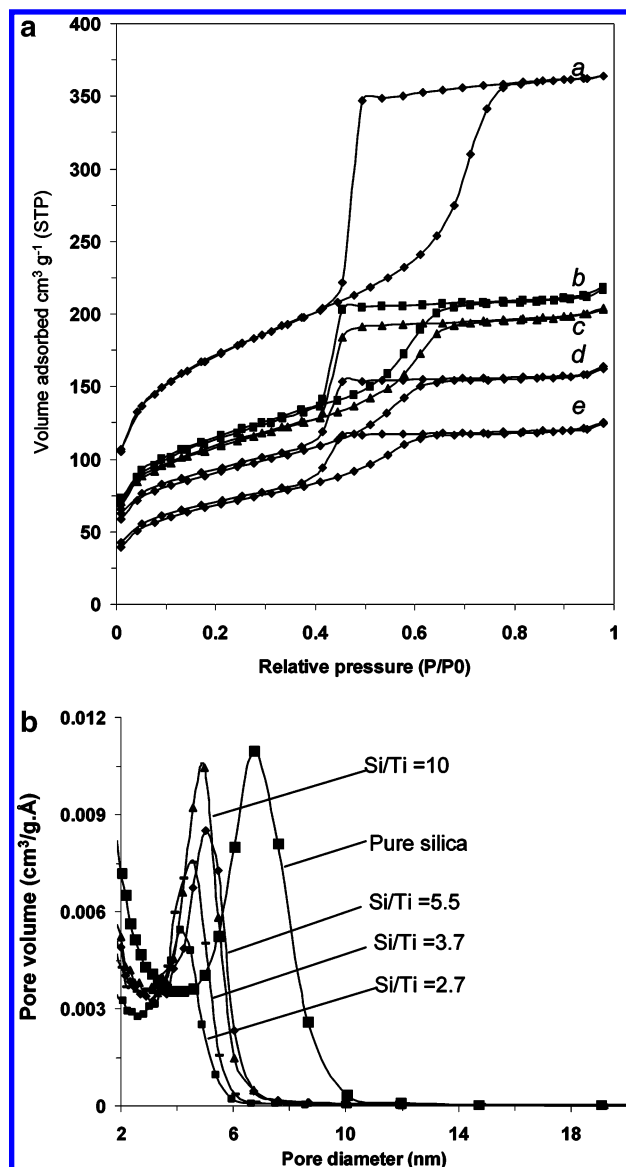


**Figure 6.** (a) Nitrogen adsorption–desorption isotherms of the samples with different content of titania (a) pure silica, (b) Si/Ti = 10, (c) Si/Ti = 5.5, (d) Si/Ti = 3.7, (e) Si/Ti = 2.7. (b) Pore size distribution of the mesoporous mixed silica–titania.

**TABLE 1: Representative Results of  $\text{N}_2$  Adsorption Experiments, Based on BET Calculations**

sample (molar ratio Si/Ti)	vol of saturation absorbed ( $\text{cm}^3/\text{g}$ ) STP	surface area ( $\text{m}^2/\text{g}$ )	pore vol ( $\text{cm}^3/\text{g}$ )	ave pore diameter (nm)	peak pore diameter (nm)
pure silica	364	589	0.56	4.7	6.8
10	220	392	0.34	3.9	4.9
5.5	205	370	0.31	3.8	5.0
3.7	159	311	0.25	3.6	4.6
2.7	125	239	0.19	3.5	4.2

higher and steeper for the pure silica sample. Pore-size distributions obtained from BJH analysis of the adsorption isotherms are shown in Figure 6b. In general, the pore size distributions indicate that all of the samples possess sharp mesopore ordering and a narrow pore size distribution, a conclusion supported by the TEM in Figure 1. Any structural changes resulting from Ti introduction are not necessarily at the expense of pore uniformity.

Decreases in the volume of saturation absorption, surface area, and pore volume are observed with increasing Ti content (Table 1) for the samples calcined at 600 °C. There is a systematic drop in saturation volume and, more importantly, pore volume with increasing Ti content. A general decrease in the peak pore diameters is also observed, with the peak pore diameter ranging from 4.2 to 5.0 nm for the Si–Ti mixed oxides compared to 6.8 nm for pure silica, which is a possible explanation for the decrease in both pore volume and saturation absorbed volume. It is logical to conclude that the TiO<sub>2</sub> crystallites are growing inside the pores during calcinations, contributing to the decrease in their effective volume and diameter. From the present data it is not possible to eliminate the possibility that some TiO<sub>2</sub> may nucleate within the silica matrix, although this configuration might be expected to be less stable.

Mixed silica–titania oxides were tested as supports for gold catalysts. It is known that the activity of gold catalysts is related to the Au particle size, Au oxidation state, and the nature of the support material.<sup>7,23,58–61</sup> The support can be of key importance for the catalytic activity of gold catalysts, as evidenced by recent results where we have found pronounced differences between gold on a titania surface compared to Au on a functionalized silica surface.<sup>22,62,63</sup> Gold was loaded onto the mixed oxide support by the DP (deposition–precipitation) method described in a previous section without heat-treatment following the DP. The activity of the gold catalyst for CO oxidation was characterized using a plug-flow reactor with a reactant stream of 1% CO–dry air at a space velocity of 40 000 cm<sup>3</sup>/(g cat.·h).<sup>22</sup> Lightoff curves were measured for the catalyst prepared by Au DP onto the calcined silica–titania sample with a molar ratio of Si/Ti = 5.5, as shown in Figure 7a. Table 2 lists the temperature at which 50% conversion is achieved for the mixed oxide support prepared with various calcination temperatures. The activity of the gold nanoparticles for carbon monoxide oxidation is clearly sensitive to the variation in the support and the well-crystalline titania obviously leads to the highest catalytic activity. Work is underway to provide complete characterization of the series of supported materials for the catalytic performance of gold nanoparticles. A typical TEM image of the catalytically active sample, shown in Figure 7, indicates that gold particles with diameters less than 3 nm were uniformly dispersed on the support surfaces, which further confirms that gold can be efficiently deposited on the support by the deposition–precipitation method after incorporating titania on the silica matrix.<sup>22,24</sup>

From the available data, the following model of the synthesis of these materials is proposed (Scheme 1). The triblock copolymer acts as a structure-directing agent and complex ligand. It is well-documented that titanium ethoxide hydrolyzes faster than TEOS. Therefore, during gelation the multivalent titanium (IV) species can associate preferentially with the hydrophilic poly(ethylene oxide) (PEO) moieties mediated by HCl.<sup>9</sup> Subsequent hydrolysis, cross-linking, and polymerization of TEOS occur to form the mesoscopically ordered inorganic/block-copolymer composites. After calcination, the titanium is efficiently positioned at the surfactant–silica interface at which the final inorganic network formation occurs. Only a portion of the Ti ions can insert into the silica framework using a block polymer as the structure-directing agent,<sup>64</sup> leading to well-dispersed titanium oxide in the silica wall, as shown in Scheme 1. The fact that there are no distinguishable peaks in the wide-angle region of the XRD pattern (molar ratio Si/Ti = 5.5, calcined at 500 °C), as shown in Figure 4, suggests that the product is an amorphous but nearly homogeneous matrix with

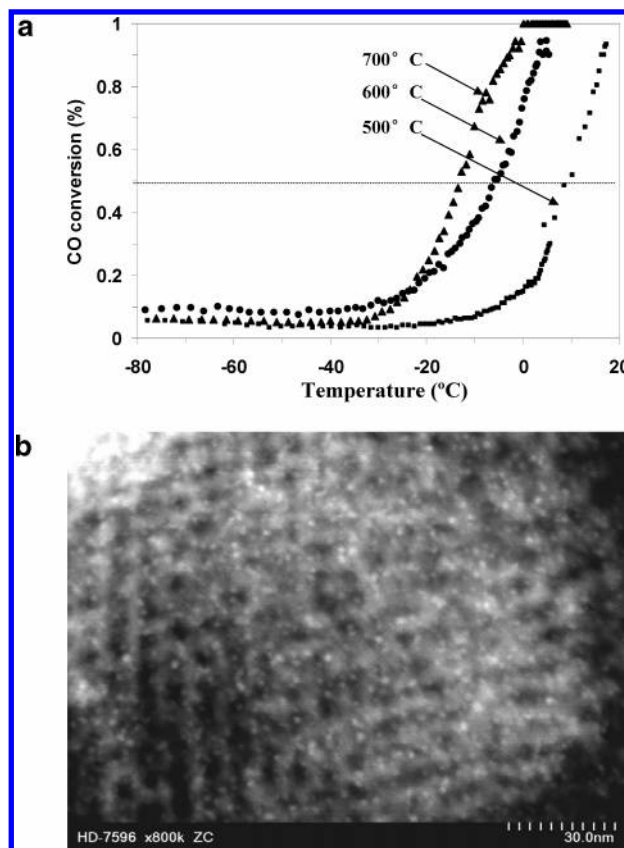


**Figure 7.** (a) Conversion of CO as a function of reaction temperature for silica–titania supports (Si/Ti = 5.5) calcined at various temperature with gold deposition–precipitation. (b) TEM images of Au supported on the mesoporous titania–silica (Si/Ti = 5.5) with calcined at 600 °C after measuring catalytic property.

**TABLE 2: Temperature for 50 % Conversion of CO over the Mixed SiO<sub>2</sub>–TiO<sub>2</sub> Support (Si/Ti = 5.5) Calcined at Various Temperatures with Gold Deposition–Precipitation**

sample	support calcination temp (°C)	temp for 50% conversion (°C)
1	500	9.0
2	600	–5.0
3	700	–13.0

ordered mesopores. Such stabilization effects would not be expected from bulk titania, indicating that titania is homogeneously associated with the silica surface. In other reports of the direct incorporation of Ti during synthesis of mesoporous titanasilicates, the ordered framework progressively deteriorated with increasing Ti/Si ratio.<sup>65–67</sup> In fact, no samples with a titanium content greater than 3 wt % have exhibited well-ordered mesostructure.<sup>68</sup> It is believed that the presence of titanium atoms inside the framework introduces defects that can lead to collapse of the framework. In contrast, the current method affixes the titania to the silica surface so that the framework is not weakened by heteroatoms. As a result, the random nucleation and growth of anatase crystals can readily occur while the ordered mesostructure is preserved.

In conclusion, we present the successful synthesis of a highly ordered, mesoporous silica–titania mixed metal oxide monolith. Templating of polymer gels with mixed sol–gel precursor solutions leads to the generation of monolithic mixed metal oxide networks, with highly uniform pore systems. The presence of templates in the channels effectively prevents agglomeration and efficiently disperses the titanium throughout the system, as confirmed by elemental mapping in TEM. N<sub>2</sub> adsorption



experiments and XRD patterns corroborate the conclusion that titania is present on the silica matrix. It was shown that the addition of titania to the silica significantly decreased the surface area and volume of pores compared to that of the pure silica material. Depending on the Si/Ti ratios, different crystalline and amorphous oxide phases were obtained. With an increase in the amount of titania or in the calcination temperature, amorphous titania gradually crystallized and formed a crystalline anatase TiO<sub>2</sub> phase, the presence of which influences the catalytic performance of gold catalysts. Diffuse reflectance UV–vis experiments and Raman spectra further confirmed that titania is present as small crystallites of anatase. This methodology provides an alternative to the direct synthesis of complex mesoporous metal oxide monoliths and coassembly of metal oxide crystalline nanophase and mesoporous materials. Therefore, the combination of binary metal oxide material synthesis with the polymer gel templating technique can lead to interesting catalytic support materials with an otherwise inaccessible combination of properties, such as excellent transport behavior, large porosity, and high specific surface area, which result in improved catalytic performance. Further catalytic studies are currently under way.

**Acknowledgment.** This work was supported by the Office of Basic Energy Sciences, U.S. Department of Energy. The Oak Ridge National Laboratory is managed by UT-Battelle, LLC, for the U.S. DOE under Contract DE-AC05-00OR22725. This research was supported in part by an appointment for H.Z. to the ORNL Research Associates Program, administered jointly by ORNL and the Oak Ridge Institute for Science and Education.

## References and Notes

- (1) Fujishima, A.; Honda, K. *Nature* **1972**, 238, 37.
- (2) Schindler, W.; Kisch, H. *J. Photochem. Photobiol. A: Chem.* **1997**, 103, 257.
- (3) Licht, S. *J. Phys. Chem. B* **2001**, 105, 6281.
- (4) O'Regan, B.; Gratzel, M. *Nature* **1991**, 353, 737.
- (5) Zhang, Z. B.; Wang, C. C.; Zakaria, R.; Ying, J. Y. *J. Phys. Chem. B* **1998**, 102, 10871.
- (6) Yu, J. C.; Lin, J.; Kwok, R. W. M. *J. Phys. Chem. B* **1998**, 102, 5094.
- (7) Haruta, M. *Catal. Today* **1997**, 36, 153.
- (8) Kresge, C. T.; Leonowicz, M. E.; Roth, W. J.; Vartuli, J. C.; Beck, J. S. *Nature* **1992**, 359, 710.
- (9) Yang, P.; Zhao, D.; Margolese, D. I.; Chmelka, B. F.; Stucky, G. D. *Nature* **1998**, 396, 152.
- (10) Yanagisawa, T.; Shimizu, T.; Kuroda, K.; Kato, C. *Bull. Chem. Soc. Jpn.* **1990**, 63, 988.
- (11) Tanev, P. T.; Pinnavaia, T. J. *Science* **1995**, 267, 865.
- (12) Zhao, D.; Feng, J.; Huo, Q.; Melosh, N.; Fredrickson, G. H.; Chmelka, B. F.; Stucky, G. D. *Science* **1998**, 279, 548.
- (13) Soler-illia, G. J. D.; Sanchez, C.; Lebeau, B.; Patarin, J. *Chem. Rev.* **2002**, 102, 4093.
- (14) Crepaldi, E. L.; Soler-illia, G. J. D. A.; Grosso, D.; Cagnol, F.; Ribot, F.; Sanchez, C. *J. Am. Chem. Soc.* **2003**, 125, 9770.
- (15) Tanev, P. T.; Chibwe, M.; Pinnavaia, T. J. *Nature* **1994**, 368, 321.
- (16) Murugavel, R.; Roesky, H. W. *Angew. Chem., Int. Ed. Engl.* **1997**, 36, 477.
- (17) Jarupatrakorn, J.; Tilley, T. D. *J. Am. Chem. Soc.* **2002**, 124, 8380.
- (18) Ogawa, M.; Ikeue, K.; Anpo, M. *Chem. Mater.* **2001**, 13, 2900.
- (19) Zhao, D.; Huo, Q.; Feng, J.; Chmelka, B. F.; Stucky, G. D. *J. Am. Chem. Soc.* **1998**, 120, 6024.
- (20) Yang, P.; Zhao, D.; Margolese, D. I.; Chmelka, B. F.; Stucky, G. D. *Chem. Mater.* **1999**, 11, 2813.
- (21) Haruta, M. *Catal. Today* **1997**, 36, 153.
- (22) Yan, W.; Chen, B.; Muhrin, S. M.; Hagaman, E. D.; Dai, S.; Overbury, S. H. *J. Phys. Chem. B* **2004**, 108, 2793.
- (23) Davis, R. J. *Science* **2003**, 301, 926.
- (24) Stangland, E. E.; Stavens, K. B.; Andres, R. P.; Delgass, W. N. *J. Catal.* **2000**, 191, 332.
- (25) Attard, G. S.; Glyde, J. C.; Goltner, C. J. *Nature* **1995**, 378, 366.
- (26) Melosh, N. A.; Lipic, P.; Bates, F. S.; Wudl, F.; Stucky, G. D.; Fredrickson, G. H.; Chmelka, B. F. *Macromolecules* **1999**, 32, 4332.
- (27) Feng, P.; Bu, X.; Stucky, G. D.; Pine, D. J. *J. Am. Chem. Soc.* **2000**, 122, 994.
- (28) Zhu, H.; Jones, D. J.; Zajac, J.; Roziere, J.; Dutartre, R. *Chem. Commun.* **2001**, 2568.
- (29) Lu, Y.; Ganguli, R.; Drewien, C. A.; Anderson, M. T.; Brinker, C. J.; Gong, W.; Guo, Y.; Soye, H.; Dunn, B.; Huang, M. H.; Zink, J. I. *Nature* **1997**, 389, 364.
- (30) Yang, P.; Zhao, D.; Chmelka, B. F.; Stucky, G. D. *Chem. Mater.* **1998**, 10, 2033.
- (31) Kortum, G. *Reflectance Spectroscopy*; Springer-Verlag: New York, 1969.
- (32) Dag, Ö.; Ozin, G. A.; Yang, H.; Reber, C.; Bussiere, G. *Adv. Mater.* **1999**, 11, 474.
- (33) Leon, R.; Margolese, D.; Stucky, G. D.; Petroff, P. M. *Phys. Rev. B* **1995**, 52, 2285.
- (34) Aronson, B. J.; Blanford, C. F.; Stein, A. *Chem. Mater.* **1997**, 9, 2842.
- (35) Zhang, W. H.; Shi, J. L.; Wang, L. Z.; Yan, D. S. *Chem. Mater.* **2000**, 12, 1408.
- (36) Garcia, C.; Zhang, Y.; DiSalvo, F.; Wiesner, U. *Angew. Chem., Int. Ed.* **2003**, 42, 1526.
- (37) Mulukutla, R. S.; Asakara, K.; Namba, S.; Iwasawa, Y. *Chem. Commun.* **1998**, 1425.
- (38) Zhang, Z. T.; Konduru, M.; Dai, S.; Overbury, S. H. *Chem. Commun.* **2002**, 2406.
- (39) Ammundsen, B.; Jones, D. J.; Roziere, J.; Burns, G. R. *Chem. Mater.* **1997**, 9, 3236.
- (40) Li, D. L.; Zhou, H. S.; Honma, I. *Nat. Mater.* **2004**, 3, 65.
- (41) Brinker, C. J.; Scherer, G. W. in *Sol–Gel Science*; Academic: San Diego, 1990.
- (42) Husing, N.; Launay, B.; Doshi, D.; Kickelbick, G. *Chem. Mater.* **2002**, 14, 2429.
- (43) Celik, O.; Dag, Ö. *Angew. Chem., Int. Ed.* **2001**, 40, 3800.
- (44) Kipkemboi, P.; Fogden, A.; Alfredsson, V.; Flodstrom, K. *Langmuir* **2001**, 17, 5398.
- (45) Yu, C. Z.; Tian, B. Z.; Fan, J.; Stucky, G. D.; Zhao, D. Y. *J. Am. Chem. Soc.* **2002**, 124, 4556.
- (46) Luan, Z.; Maes, E. M.; Heide, P. A. W.; Zhao, D.; Czernuszewicz, R. S.; Kevan, L. *Chem. Mater.* **1999**, 11, 3680.
- (47) Widenmeyer, M.; Grasser, S.; Kohler, K.; Anwender, R. *Microporous Mesoporous Mater.* **2001**, 44–45, 327.
- (48) Ranade, M. R.; Navrotsky, A.; Zhang, H. Z.; Banfield, J. F.; Elder, S. H.; Zaban, A. J.; Borse, P. H.; Kulkarni, S. K.; Doran, G. S.; Whitefield, H. J. P. *Natl. Acad. Sci. U.S.A.* **2002**, 99, 6476 suppl.
- (49) Klug, H. P.; Alexander, L. E. *X-ray Diffraction Procedures*; John Wiley & Sons: New York, 1959.
- (50) Rainho, J. P.; Rocha, J.; Carlos, L. D.; Almeida, R. M. *J. Mater. Res.* **2001**, 16, 2369.
- (51) Srinivasan, S.; Datye, A. K.; Hampden-Smith, M.; Wachs, I. E.; Deo, G.; Jehng, J. M.; Turek, A. M.; Peden, C. H. F. *J. Catal.* **1991**, 131, 260.
- (52) Henglein, A. *Chem. Rev.* **1989**, 89, 1861.
- (53) Liu, Z.; Davis, R. J. *J. Phys. Chem.* **1994**, 98, 1253.
- (54) Gao, X.; Wachs, I. E. *Catal. Today* **1999**, 51, 233.
- (55) Hutter, R.; Mallat, T.; Baiker, A. *J. Catal.* **1995**, 153, 177.
- (56) Kosuge, K.; Singh, P. S. *J. Phys. Chem.* **1999**, 103, 3563.
- (57) Kruk, M.; Jaroniec, M. *Chem. Mater.* **2001**, 13, 3169.
- (58) Valden, M.; Lai, X.; Goodman, D. W. *Science* **1998**, 281, 1647.
- (59) Oh, H. S.; Yang, J. H.; Costello, C. K.; Wang, Y. M.; Bare, S. R.; Kung, H. H.; Kung, M. C. *J. Catal.* **2002**, 210, 375.
- (60) Guzman, J.; Gates, B. C. *J. Am. Chem. Soc.* **2004**, 126, 2672.
- (61) Arrii, S.; Morfin, F.; Renouprez, A. J.; Rousset, J. L. *J. Am. Chem. Soc.* **2004**, 126, 1199.
- (62) Overbury, S. H.; Ortiz-Soto, L.; Zhu, H.; Lee, B.; Amiridis, M. D.; Dai, S. *Catal. Lett.* **2004**, 95, 99.
- (63) Zhu, H.; Lee, B.; Overbury, S. H.; Dai, S. *Langmuir* **2003**, 19, 3974.
- (64) Zhang, W.; Lu, J.; Han, B.; Li, M.; Xiu, J.; Ying, P.; Li, C. *Chem. Mater.* **2002**, 14, 3413.
- (65) Alba, M. D.; Luan, Z.; Klinowski, J. *J. Phys. Chem.* **1996**, 100, 2178.
- (66) Mokaya, R. *J. Phys. Chem.* **2000**, 104, 8279.
- (67) Blasco, T.; Corma, A.; Navarro, M. T.; Perez-Pariente, J. *J. Catal.* **1995**, 156, 65.
- (68) Gontier, S.; Tuel, A. *Zeolites* **1995**, 15, 601.